Synthesis of Yttrium Doped Barium Zirconate/Cerate Electrolyte Materials and Densification Using Conventional and Cold-Sintering Processes

Pablo Castellani, Eric Quarez, Clement Nicollet, Olivier Joubert, Annie Le Gal La Salle

To cite this version:

Pablo Castellani, Eric Quarez, Clement Nicollet, Olivier Joubert, Annie Le Gal La Salle. Synthesis of Yttrium Doped Barium Zirconate/Cerate Electrolyte Materials and Densification Using Conventional and Cold-Sintering Processes. ECS Transactions, 2022, 109 (13), pp.13-29. ⟨10.1149/10913.0013ecst⟩. ⟨hal-04266398⟩

HAL Id: hal-04266398
https://hal.science/hal-04266398v1

Submitted on 6 Nov 2023

Synthesis of Yttrium Doped Barium Zirconate/Cerate Electrolyte Materials and Densification Using Conventional and Cold-Sintering Processes

P. Castellani, E.Quarez, C. Nicollet, O. Joubert and A. Le Gal La Salle

Nantes Université, CNRS, Institut des Matériaux de Nantes Jean Rouxel, IMN, 2 rue de la Houssinière, F-44000 Nantes, France

Compared to high temperature solid oxide electrolysis cell, usually based onYttrium stabilized Zirconia electrolytes, intermediate temperature proton conducting electrolysis cell, allows the production of water free hydrogen and a better chemical stability. Proton conducting perovskite materials, such as Barium Indates, Zirconates or Cerates are nearly commercial electrolytes for such devices. At intermediate temperature and under humid atmosphere, hydration process allows diffusion of protonic charges. Such electrolyte material combines a low thermal expansion coefficient and a high protonic conductivity. and The Zirconium rich material $BaZr_{0.7}Ce_{0.2}Y_{0.1}O_{3-\delta}$ that shows a conductivity around 10^{-2} $S.cm^{-1}$ at 500°C will be compared to the Cerium rich $BaZr_{0.3}Ce_{0.6}Y_{0.1}O_{3-\delta}$ material that shows conductivities around 10^{-4} $S.cm^{-1}$ at the same temperature.

INTRODUCTION

With their high energy conversion and low material impact on the environment, solid oxide electrolysis cells embody the perfect device to perform highly efficient water electrolysis. The first SOEC's generation was mainly based on anionic-conducting electrolytes materials such as Yttria-stabilized zirconia (YSZ). However, these devices were showing some stability and reliability issues due to their high operating temperatures exceeding 800°C. Therefore, a second generation of devices based on protonic-conducting electrolytes led to intermediate operating temperatures around 450-600°C. Iwahara (1) developed the initial concept of this steam electrolyze using proton-conducting electrolytes, based on perovskite-type materials. Under these temperatures, specific perovskite-type (Ba,Sr,La) $(Zr,Ce,In)O_3$ (2-6) oxides showed promising protonic conduction in humid-air atmospheres.

The proton conducting SOECs show the advantage of a hydrogen electrode side that is only submitted to hydrogen outflow. And an air electrode side which is only submitted to the steam inflow and oxygen outflow. Thus, without the steam atmosphere on the hydrogen side, it is possible to avoid the fuel dilution (7).

For a large panel of perovskites-type (ABO_3) materials, the reaction that forms the protonic defect at moderate temperature is the adsorption and dissociation of water (8). This reaction is made possible thanks to the presence of oxide ion vacancies that are naturally present inside the perovskite, issued from the presence of the cationic elements. Moreover, these vacancies can also be formed, based on the addition of doping elements into the structure. Thanks to these defects, the water gas phase is dissociated into a hydroxide and a proton. The vacancies are then filled with hydroxide ions. The remaining proton bonds with the oxygen lattices. This reaction is represented by the Kroger-Vink equation [1].

$$H_2O_{(gas)} + V_{\ddot{O}} + O_o^x \rightleftharpoons OH_{\dot{o}} \qquad [1]$$

Ceramic based Barium Zirconate and Barium Cerate were suitable and innovative materials as solid oxides proton-conducting electrolytes. However, despite showing very high protonic conductivity, Barium Cerates encounters thermochemical stability issues. This instability is mainly due to the high reactivity of cerium to carbon dioxide (9). On the contrary, Barium Zirconate are extremely stable at high temperature, but shows low protonic conductivity. Because Barium Cerate and Barium Zirconate can easily mix to form a solid solution, it is possible to incorporate a certain amount of Cerium inside the Barium Zirconate perovskite lattice, leading to a composite material that exhibits sufficient thermochemical stability and adequate protonic conductivity (10). The chemical stability of the composite towards carbon dioxide is increasing with high zirconium content. The Ce-substituted Barium Zirconate can also be doped with several rare earth materials. Kreuer (11) reported that Yttrium doping enhance the formation of oxygen vacancies and ease the substitution process, while guarantying protonic conductivity. This study focuses on the powder synthesis of the solid oxide electrolyte of general formula $BaZr_{1-x}Ce_xY_{0.1}O_{3-\delta}$ electrolyte along with its characterization and densification. This material exhibits high protonic conductivity under hydrogen atmosphere at intermediate temperature. However, Merkle and Maiers (12) showed that, at high temperature it is possible to observe an anionic, protonic, and electronic mixed conduction.

Our work focuses on the $BaZr_{0.7}Ce_{0.2}Y_{0.1}O_{3-\delta}$ specific stoichiometry. The Zirconium rich phase has been chosen for its thermochemical reliability under carbon dioxide, which might allow CO_2/H_2O co-electrolysis (13). Moreover, by avoiding a too large amount of cerium inside the lattice, this specific stoichiometry reduces the presence of electronic conductivity at intermediate temperature. Indeed, the Ce^{4+} is submitted to a redox reaction causing its own reduction in Ce^{3+} (14), which induce an intrinsic movement of electrons. However, a certain amount of Cerium is still mandatory to keep a decent protonic conductivity.

The $BaZr_xCe_{1-x}Y_{0.1}O_{3-\delta}$ zirconium rich phase is synthetized by glycine-nitrate combustion process, which is the present method used in the industry (15-16). This method guarantees a nano-sized powders synthesis. This last point is crucial to our work since the morphology of the powder has a primary impact on the efficiency of the sintering process. In fact, the higher is the specific area of the powder, the more efficient the coarsening effect will be (17). By reducing the porosity and the presence of grain boundary resistance, the conductivity of the material can be improved. To do so, the electrolyte material must be shaped into pellets and highly densified (90% ≤ compactness). These high compacity requires very high sintering temperature (1600-1800°C), even more with the zirconium rich components since Zirconia has one of the highest thermal refraction coefficients known, around $9.7\ 10^{-6}K^{-1}$ (18). To reduce the very high temperature requested for the Zirconate densification, several methods exist. Such as, sintering aids like zinc oxide can be added (19-20). However, the addition of a transition metal into the lattice must remain very low, because its presence improves the electronic conductivity contribution. Anothertechnique used is the cold-sintering process, firstly described by Randall (21-23). It consists in the incorporation of a small quantity of solvent, water, ethanol, or acetone intothe ceramic powder. The solvent dissolves a part of the powder and infiltrate the space between the different grains. With the increase of the pressure and the temperature, the solvent will undergo cycling state variations, evaporation fix the infiltrated powder between the grains, and precipitation dissolves more powder and infiltrate it between the grain. The solvent evaporation will generate a super-saturation of ceramics on the edges of the grains, which will lead to an epitaxial growth. After a given time at intermediate temperature, the solvent will be fully evaporated, and the cold-sintering effect will end.

The specific stoichiometry of $BaZr_{0.7}Ce_{0.2}Y_{0.1}O_{3-\delta}$ is an innovative material that will improve the development of proton conducting electrolysis cells. A first part of the study will focus on the synthesis and the characterization of the new electrolyte material. A second part will focus on electrochemical characterization of the electrolyte material. Finally, the performances of the $BaZr_{0.7}Ce_{0.2}Y_{0.1}O_{3-\delta}$ will be compared to the Cerium rich $BaZr_{0.3}Ce_{0.6}Y_{0.1}O_{3-\delta}$ material.

EXPERIMENTAL

The electrolyte material of $BaZr_{0.7}Ce_{0.2}Y_{0.1}O_{3-\delta}$ has been synthetized by self-combustion reaction. First the nitrate precursors and the glycine are dissolved into deionized water which leads to an acidic solution. The pH of the solution is then neutralized by ammonia addition. During this step, a white zirconium hydroxide precipitate is formed (24). After the total dehydration of the final solution, a crystallized gel is obtained. This gel is heated at 350°C, to trigger the auto-combustion reaction. A very thin powder is obtained after the combustion. The synthesis reaction is described by the following equation:

$$\begin{aligned} & Ba(NO_3)_2 + 0.7ZrO(NO_3)_2 + 0.2Ce(NO_3)_3 + 0.1Y(NO_3)_3 + xC_2H_5NO_2 \\ & \rightarrow BaZr_{0.7}Ce_{0.2}Y_{0.1}O_{2.95} + 2xCO_2 + 2.5xH_2O + (0.5x + 2.45)N_2 + (5.925 \\ & \quad - 2.25x)O_2 \end{aligned} \qquad [2]$$

To get rid of all the unburned organic leftovers, and to avoid the presence of barium carbonate in the material, the powders undergo a calcination treatment at 1100°C for 10h. The calcined powder is then manually milled in a mortar, to break the big agglomerates. The thin powder is then shaped into 10 mm diameter pellets using a uniaxial press. The density of the pellets is linked to the force applied on the powder. However, if a to high force is applied (>750 MPa), the pellets might break. The last step consists in the sintering of the formed pellet, under air at 1600°C for 12h. For crystallographic purpose, the entire solid solution of the $BaZr_xCe_{1-x}Y_{0.1}O_{3-\delta}$ has been synthetized, by steps of 0.1 for Zr(x), using the synthesis process described above.

One of the main goals is to reduce the electrolyte material sintering temperature. A first attempt considered the regulation of the fuel/oxidizer ratio, to optimize the grain size and the crystallinity of the phase. A second attempt focused on the calcination treatment of the powder. Indeed, several heat treatments have been tested at 900°C, 1000°C and 1100°C. After the calcination process, the grain size of the calcined powders has been reduced by planetary ball milling in zirconia jars for 1h at 500rpm. Another solution consists in using sintering aids like zinc oxide, to enhance the cation diffusion during the sintering process, thus reducing the sintering temperature. However, despite its efficiency,this method tends to add an inconvenient amount of electronic conductivity to the electrolyte. Finally, one solution has been to use the Cold Sintering Process (CSP). CSP ismade possible using a heating jacket. This jacket is set around the pelletizer in the uniaxialpress. The setup is heated at 180°C during 1h. Using this method, the sintering temperaturecan be lowered, while reaching compactness equivalent to the conventional sintering.

The morphology of the powders obtained after the different heat treatments have been characterized. For the grain size measurements, the laser-granulometry (Masterize2000) was used in both pressurized air and absolute ethanol ultrasonic bath. The specific surface areas were determined using the Brauner, Emmett and Teller (BET) method (Micrometrics 3flex). The presence of the impurities in the raw powder have been observed using simultaneous Thermogravimetric Analysis (TGA) and Differential Scanning Calorimetry (DSC). The powder shape and the pellet surface have been characterized using the Scanning Electron Microscopy (JEOL 7600 SEM) and Energy Dispersive X-ray spectroscopy (EDX) was performed on polished surfaces of the samples to determine the repartition of the elements in the electrolyte material. X-ray diffraction (XRD) characterization has been made on the powders, at room and high temperature (1100°C). The X-ray diagrams were recorded using a Brucker D8 advance diffractometer in Bragg-Brentano geometry. The source is made of a copper anode, that give a wavelength of $\lambda_{cu\ k\alpha 1} = 1.5406$Å in the 5-80° 2θ range covered by a 0.42s step of 0.018° size. The profile patterns were refined using the FULLPROF program. Moreover, the cell parameters and the phase proportions were determined using the Rietveld refinement on TOPAS software. The temperature dependance of the pellet dimension has been characterized by dilatometry using the NETZSCH Dil 402 C dilatometer coupled to a 1600°C Furnace. The data were collected and analyzed using the Proteus Analyzer software.

The electrochemical properties of the electrolytes pellets have been characterized by electrochemical impedance spectroscopy (EIS). The EIS measurements were performed in different atmospheres (humid-air, dry air, hydrogen) with a Solartron 1260 in a frequency range from 0.1 Hz to 1MHz. To determine the amplitude signal allowing the best noise-signal ratio for the measurements while addressing the linearity requirements a large range of amplitudes were studied from 25mV to 1V. The EIS measurements are made with symmetrical cell made of gold and $Ba_{0.5}Sr_{0.5}Co_{0.8}Fe_{0.2}O_{3-\delta}$ electrodes and $BaZr_xCe_{1-x}Y_{0.1}O_{3-\delta}$ electrolyte. The symmetrical cells were put inside an oven to study the electrochemical dependance of the temperature. The temperature ranges from 750°C to 350°C, decreasingly by 50°C steps. At each steps a 2-hour plateau is performed to reach the thermal stability of the sample. The impedance spectra of the $BaZr_{0.7}Ce_{0.2}Y_{0.1}O_{3-\delta}$ has been modelized with equivalent circuits based on R/CPE electrical components.

RESULT AND DISCUSSION

This study is based on the thesis work of Dr. K. Thabet (25), where the cerium rich phase of $BaZr_{0.3}Ce_{0.6}Y_{0.1}O_{3-\delta}$ was synthetized and characterized. Some of her results will be used as a comparison for the characterization of the zirconium rich phase which is the object of this study.

Purification of the $BaZr_{0.7}Ce_{0.2}Y_{0.1}O_{3-\delta}$ after synthesis

The $BaZr_{0.7}Ce_{0.2}Y_{0.1}O_{3-\delta}$ was synthetized by glycine-nitrate auto-combustion. As shown on Figure 1a, TGA/DSC measurements have been made. It shows a first 3% mass loss observable at around 300°C, which corresponds to the degradation of the organic materials. A second 2% mass loss is observed from 600 to 1100°C, which corresponds to the degradation of the barium carbonate (26). The presence of these different impurities has been followed by XRD characterization throughout temperature evolution. It confirms the presence of the organic impurities in the raw powder, which can be eliminated by a simple pyrolysis at 900°C. However, the Barium carbonate is still present in the phase, in accordance with the decomposition temperature of the barium carbonate of 1000°C. It is therefore necessary to reach a calcination temperature of 1100°C, as it was the case for the cerium-rich phase $BaZr_{0.3}Ce_{0.6}Y_{0.1}O_{3-\delta}$ [25].

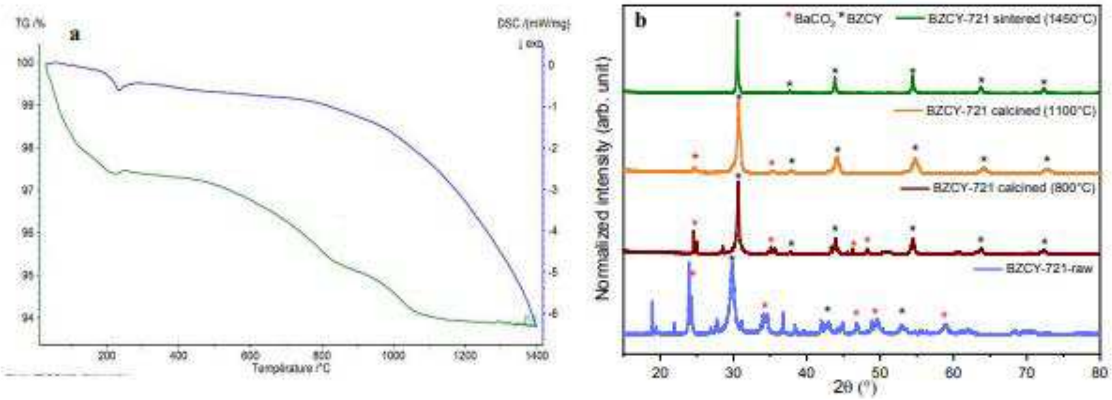

Figure 1. Decomposition of the $BaZr_{0.7}Ce_{0.2}Y_{0.1}O_{3-\delta}$ (BZCY-721) and organic leftovers characterized by TGA/DSC (a) and XRD (b)

BET measurements have been made at each heat treatment step, to follow the temperature dependance of the specific area of the powder as shown in Table1. The results show the influence of the grain coarsening on the specific area.

TABLE 1. BET measurement of the $BaZr_{0.7}Ce_{0.2}Y_{0.1}O_{3-\delta}$ powders after each heattreatment

	Powder	Specific area (g.m²)
a	raw	17.2
b	Pyrolysis	12.1
c	Calcination	8.9
d	Sintering	7.2

Morphology measurements of the synthetized powder

The morphology of the synthetized powders has a huge influence on the densification process. To enhance this densification process, the specific area of the powder should be maximized, therefore the grain size should be as small as possible (25). Powders from the three different steps (raw, calcination, sintering) have been characterized by granulometry and SEM as shown by figure 2. The raw powder shows large porous agglomerates made of very small grains. Even after ultrasonic treatment, it is impossible to differentiate the grain and the agglomerates size (10-100µm). After calcination porous agglomerates are still present in the raw powder. However, the calcination process at 1100°C the coarsening is triggered, and the powder starts to densify. This phenomenon tends to block the cation diffusion process during the sintering (27) and the particle size ranges between 3 and 30 µm. After sintering the densification process is visible: the grain boundary is harder to distinguish, even if the particle size is similar to the calcined powders' ones. This similarity can be explained by the reduction of intern porosity and the improvement of the compactness of the grains.

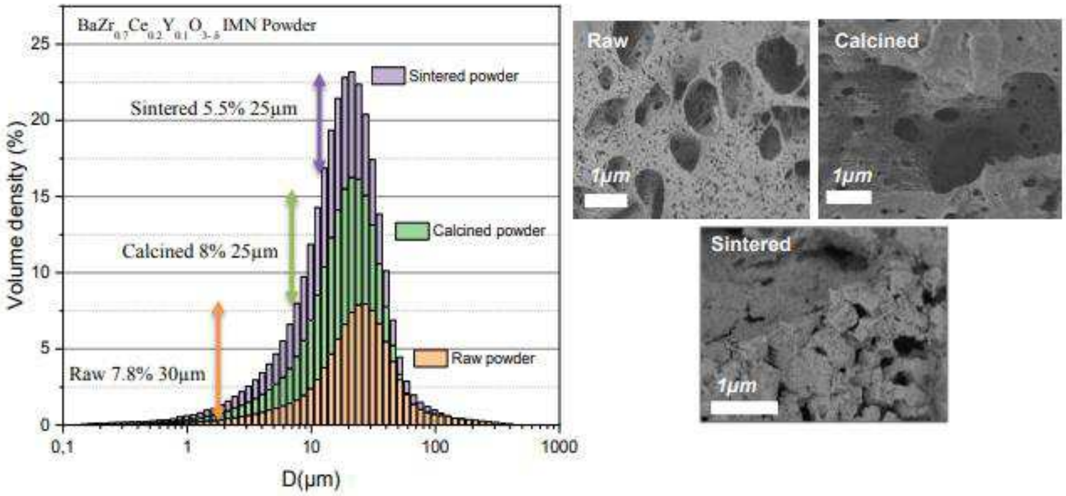

Figure 2. Morphology of the synthetized electrolyte powder, after different heat treatment, characterized by granulometry and SEM

As a basis for comparison, the morphology of the $BaZr_{0.7}Ce_{0.2}Y_{0.1}O_{3-\delta}$ commercial powder from Cerpotech has also been characterized. As shown in Figure 3, the powders present, a bimodal behavior around 10µm and below 1µm.

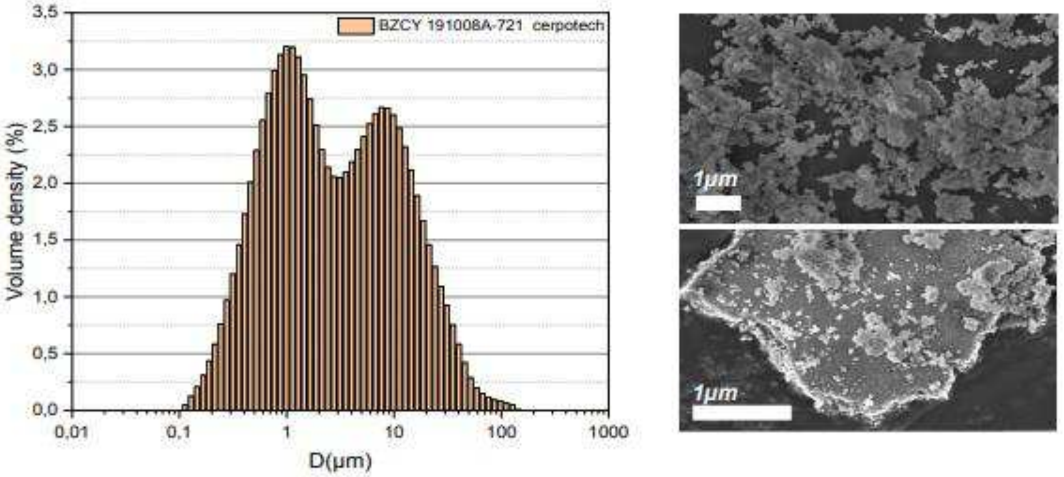

Figure 3. Morphology of the synthetized electrolyte powder, after different heat treatment, characterized by granulometry and SEM

To improve the densification process, it is necessary to decrease the particle size of the calcined $BaZr_{0.7}Ce_{0.2}Y_{0.1}O_{3-\delta}$ by broking the agglomerates. Therefore, the electrolyte powder has been milled using planetary ball milling. However, the apparition of impurities can be observed after the milling. The use of zirconia jars and absolute ethanol got rid of these impurities. The milled powder has been characterized by granulometry, and it is possible to observe a decrease of the particle size after milling. The milled powders show the presence of particle with 1µm size as shown on Figure 4. To complete the morphological study, SEM and BET measurements have also been made on the different powders. SEM images confirm the behavior of the powders. The results obtained after milling shows a bimodal behavior which indicates that the synthetized powder is similar to the commercial powder.

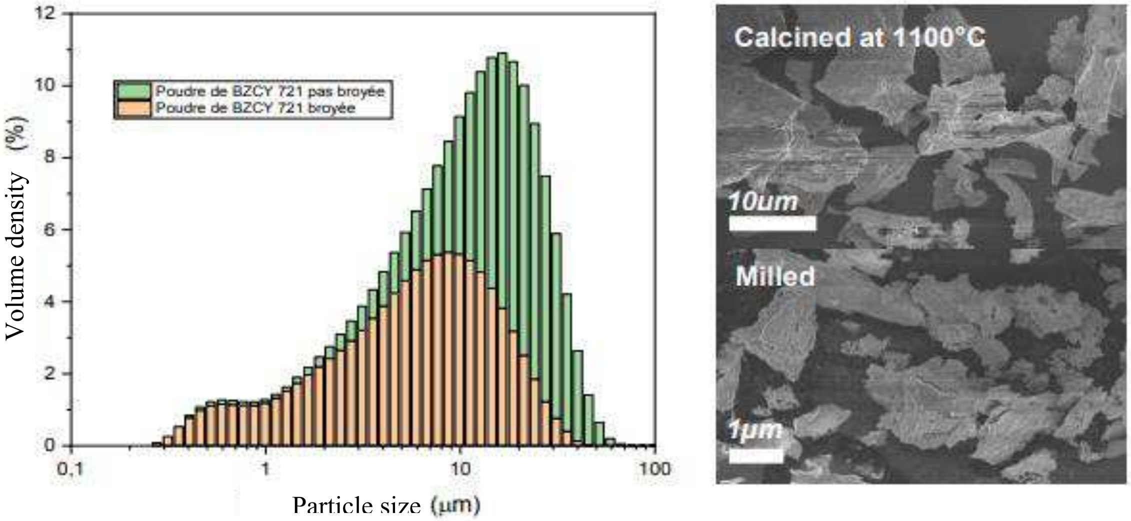

Figure 4. Morphology of the synthetized electrolyte powder, before and after ball milling characterized by granulometry and SEM

Conventional sintering and Cold-sintering process

The evolution of the powder morphology over temperature gives a better understanding of the densification process of the specific phases of the $BaZr_{0.7}Ce_{0.2}Y_{0.1}O_{3-\delta}$. Cerates and Zirconates are well known refractory materials as they are part of the ceramic family. However, the zirconate has the higher refractive coefficient (18). Therefore, the coarsening process is limited by the Zr^{4+} cation diffusion. It has been noticed that the cerium-rich pellets were able to reach 93% density at 1450°C, whereas it is necessary to reach 1600°C to obtain a 93%density with the zirconium rich pellets he evolution of the densification phenomenon has been studied using dilatometry.

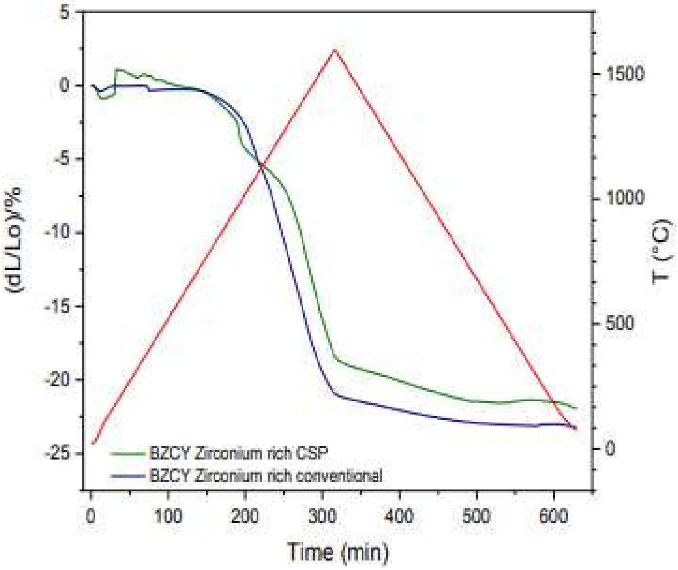

Figure 5. Dilatometry measurements comparison of $BaZr_{0.7}Ce_{0.2}Y_{0.1}O_{3-\delta}$ electrolytes based on Conventional and CSP protocol, for synthetized (a)

Figure 5 shows dilatometry measurements of different zirconium rich samples. The first part (0-150min) can be described as the thermal expansion of the frame. Thereafter the densification process is measured until the furnace reach its maximum temperature (1600°C). During the decrease of the temperature after 400 min, the decrease of the relative volume is due to the thermal withdrawal of the frame. The evolution of two electrolytes, obtained for the synthetized samples sintered respectively using the conventional protocol and using CSP, is described on Figure 5. The conventional pellet has a withdrawal around 22% where the CSP one endures a 20% withdrawal. Since the CSP triggers preliminary sintering, it is normal to measure a smaller volume withdrawal. For the cerium rich phase, the conventional sintering shows a withdrawal of 21% at 1400°C (25). For the commercial powders, the conventional electrolyte shows a 26% volume withdrawal. By comparison, it has been observed that the commercial powder is highly reactive to sintering and gives electrolytes with higher relative density. The commercial powder has higher densification potential than the powder synthetized. This could be related to the grain size described above. To go deeper into the densification potential of the material, several densification protocols have been compared and SEM images of the different electrolyte samples have been made.

TABLE 2. Compacity comparison of the Cerium rich electrolyte before and after CSP

	sample	Density (%)	Temperature (°C)	Pressure (MPa)
a	Green-Conv	65		375 - 10min
b	Green-CSP	89	180	375 - 1h
c	Sintered-CSP	93	1250 - 10h	
d	Sintered-Conv	95	1450 - 12h	

TABLE 3. Compacity comparison of the Zirconium rich electrolyte before and after CSP

	sample	Density (%)	Temperature (°C)	Pressure (MPa)
a’	Green-Conv	62		375 - 10min
b’	Green-CSP	83	180	375 - 1h
c’	Sintered-CSP	85	1450 - 10h	
d’	Sintered-Conv	93	1600 - 15h	

The zirconium rich and cerium rich pellets surface and chunk have been characterized by SEM. The densification dependance on the stoichiometry, and the sintering protocols has been compared.

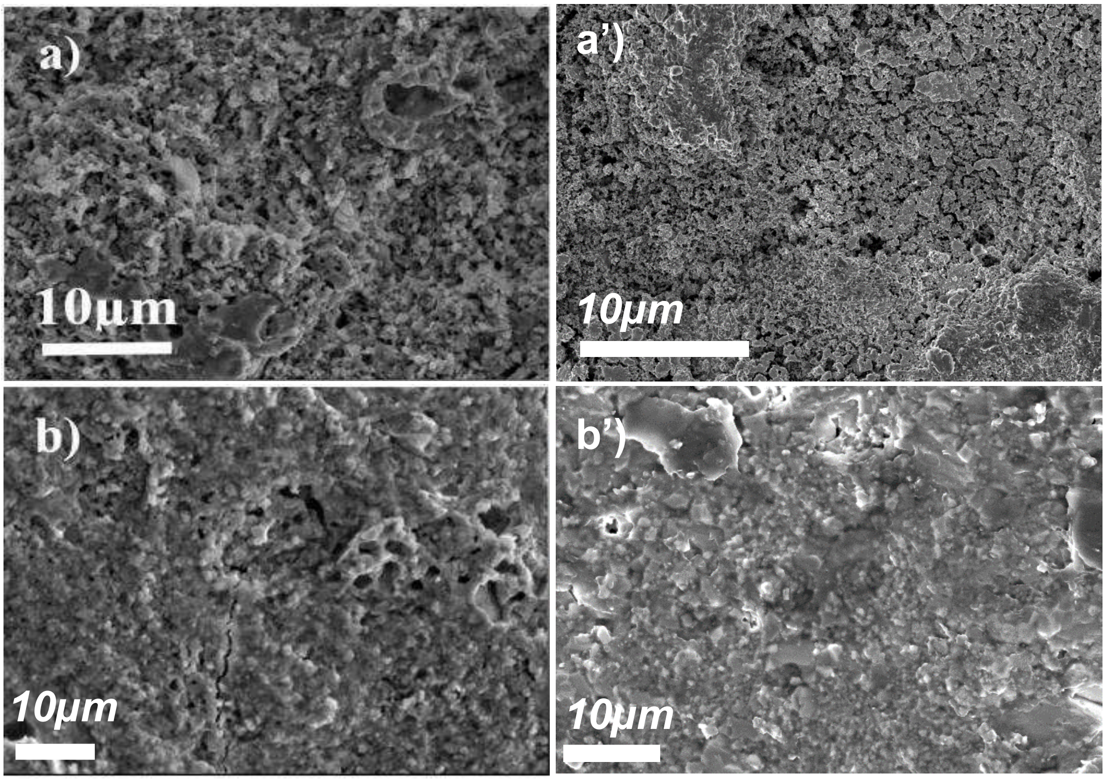

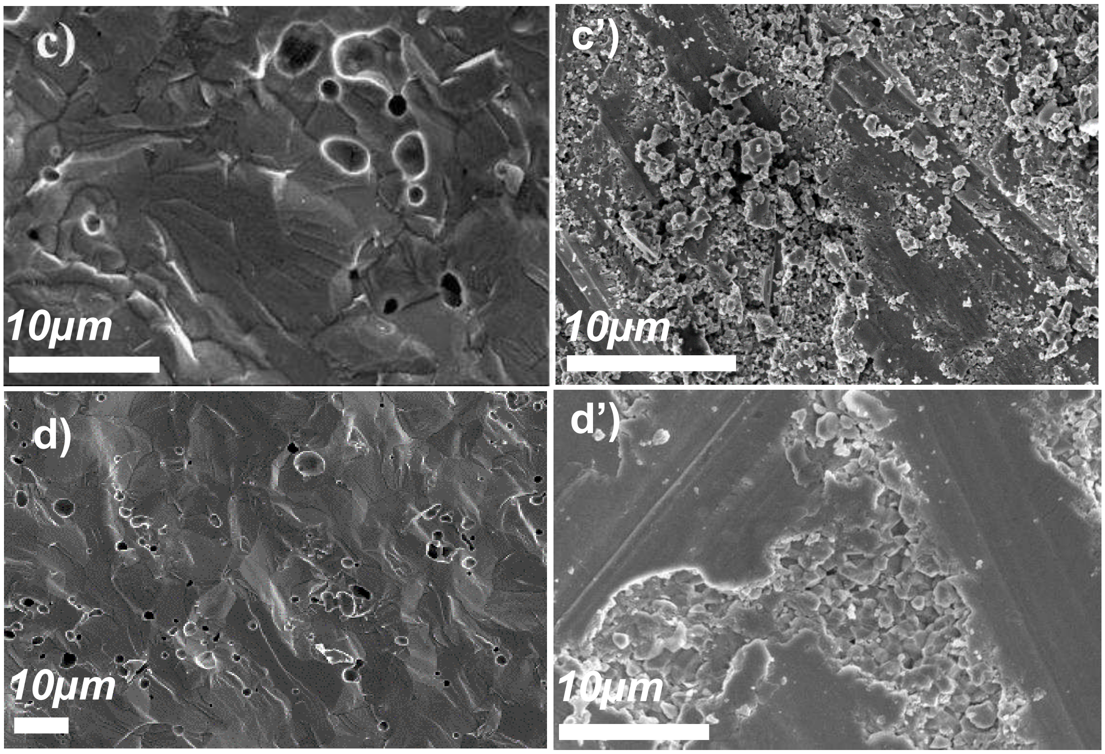

Figure 6. SEM characterization of the electrolyte pellet, after calcination (a), after calcination and CSP (b), after calcination, CSP and sintering (c), and after calcination and sintering (d) for the erium rich sample (a,b,c,d) and Zirconium rich sample (a',b',c',d')

For the green pellet, which corresponds to the electrolyte formed after uniaxial pressing and before calcination, the structure is very porous and shows a relative density between 55 (a) and 65% (a'). It is still possible to observe the grains that compose these electrolytes. After CSP grains' densification leads to relative densities of 89% (b) and 91% (b'). However, this densification is not homogeneous, and the surface still present a large amount of grain boundary. After sintering the CSP pellets (c) at 1250°C and (c') at 1450°C, the densification process is observable. For the cerium rich phase (c), the CSP process has greatly influenced the densification (93%) and allows a reduction of the sintering temperature. However, for the Zirconium rich phase (c') the structure remains porous, and the relative density does not exceed 85%. Moreover, for the Zirconium rich phase the addition of water inside the structure of the pellet produces Zirconium hydroxides which generate mechanical stress inside the pellet leading to the breakdown of the pellet upon sintering. After conventional sintering (without CSP) at 1450°C (d) and 1600°C (d'), for both stoichiometries, the densification is complete, the structure becomes homogeneous, and the grain boundary is not visible anymore. Finally, this study shows that the compacity reached for cerium rich phase, using CSP at 1250°C is close to the compacity reached by conventional sintering at 1450°C. At the opposite, for the zirconium rich stoichiometry, the CSP, leading to final breakdown of samples correlated to mechanical stress is not convenient. The addition of a solvent inside the pellet, triggers the formation of hydroxides (25). These hydroxides are blocked inside the pellet structure after the cold-sintering process, and they tend to damage the structure when they decompose at very high temperature.

XRD characterization refinement

To understand the origin of the densification and the mechanical stress induced by the CSP, which was not observed for the cerium rich phase, we have focused on the crystallinity of the $BaZr_{0.7}Ce_{0.2}Y_{0.1}O_{3-\delta}$ phase. XRD characterization shows that after sintering, there was a segregation of the Cerium and the Zirconium in the structure, leading to a double-phase material. This segregation is not observable in the case of the cerium rich $BaZr_{0.3}Ce_{0.6}Y_{0.1}O_{3-\delta}$ [25]. Figure 7a shows the structural analysis that has been made on the electrolyte powder using Le Bail and Rietveld refinements. Several space groups have been tested (Pm-3m, Imma, R-3c, Pnma).

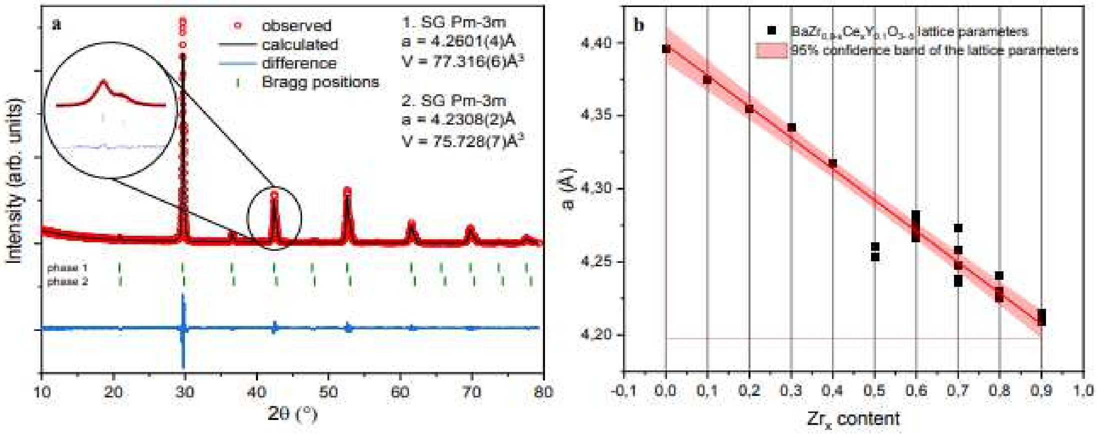

Figure 7. XRD characterization of the segregation behavior of the zirconium rich phase (a) and lattice parameter dependence to the stoichiometry following the vegard's law (b)

To study the lattice parameter dependance to the stoichiometry, the complete solid solution of the $BaZr_xCe_{1-x}Y_{0.1}O_{3-\delta}$ has been studied. Several samples have been tested, even powders coming from different laboratories and commercial powders. It has been observed that only Zirconium rich powders were subjected to this segregation leading to the crystallographic double-phase diagram. On Figure 7b, it is possible to see that the $BaZr_{0.5}Ce_{0.4}Y_{0.1}O_{3-\delta}$ and the $BaZr_{0.7}Ce_{0.2}Y_{0.1}O_{3-\delta}$ do not follow the vegard law. The difference of stoichiometry and lattices parameters within the electrolyte induces some gradient of the diffusion coefficient, which might lead to the densification issues and mechanical instability of the structure after the sintering process described above.

EIS characterization of the electrolyte material

Finally, the electrochemical properties of the electrolyte material have been characterized by EIS. The first step of this characterization has been to proceed to the linearity test to determine the voltage amplitude variation (10mV – 1V). This test is designed to obtain the best signal to noise ratio for the following electrochemical measurements. Figure 8 shows that the linearity domain is overpassed at 200mV. Therefore, a voltage amplitude of 100mV has been chosen for the following EIS characterization of the Zirconium rich electrolyte material.

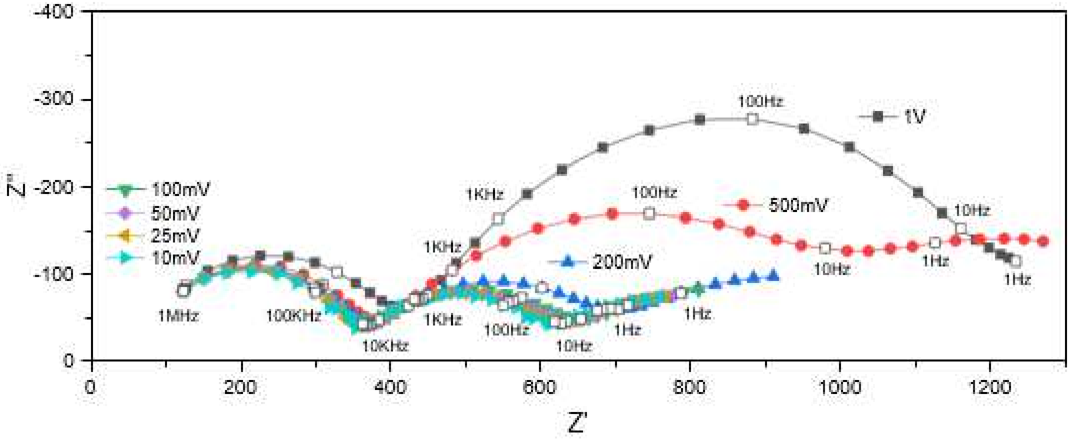

Figure 8. Determination of the linearity domain of the electrolyte by PEIS measurements

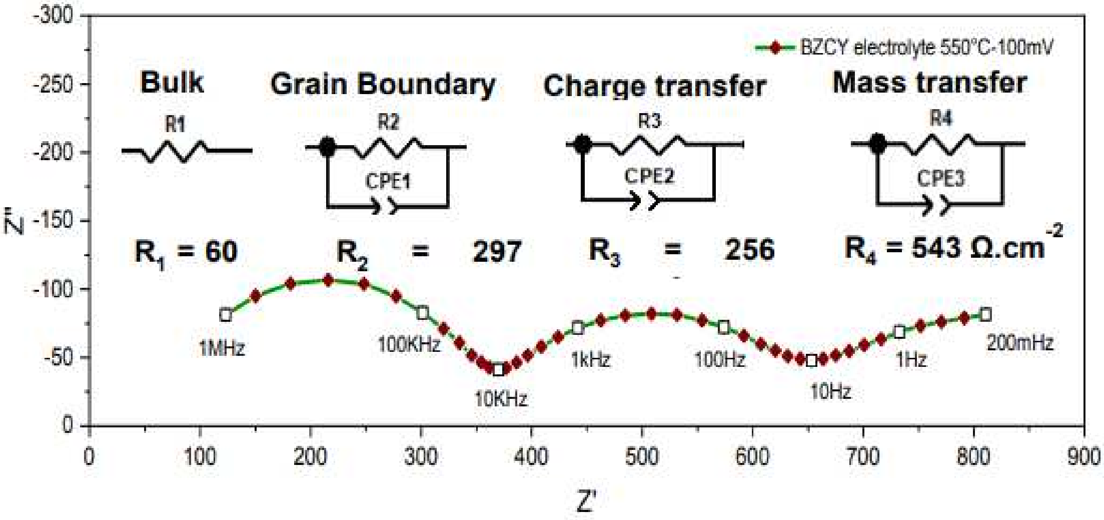

Figure 9. EIS measurement at 550°C of a symmetrical cell based on $BaZr_{0.7}Ce_{0.2}Y_{0.1}O_{3-\delta}$ electrolyte

Figure 9 shows the Nyquist diagram of the EIS measurement of the symmetrical cell Gold/$BaZr_{0.7}Ce_{0.2}Y_{0.1}O_{3-\delta}$/Gold electrodes at 550°C. It can be modelled by the equivalent circuit schematized in Figure 9, in which a resistance and three R/CPE elements are in series. The impedance of the CPE element is shown by the equation [3]

$$Z_{CPE} = \frac{1}{Q_{CPE}* \, jw^{P}} \qquad [3]$$

Were Q_{CPE} is the admittance value in rad.$s^{-1}$and where P is the eccentricity parameter of the β angle in rad. The real capacitance must be recalculated using the equation [4].

$$C_{real} = \frac{(R_{mes}*Q_{mes})^{\frac{1}{P}}}{R_{mes}} \qquad [4]$$

Were R_{mes} are the measured resistance in Ω and were Q_{mes} are the measured admittances in rad. Table 4 shows the capacitance values of R_1, R_2, R_3 and R_4 resistances attributed to the bulk, the grain boundary, the mass transfer, and the charge transfer.

TABLE 4. Values of the electrochemical measurement of the different contributions

Contribution at 550°C	Bulk R1	GB R2/C1	CT R3/C2	MT R3/C3
Resistance (Ω.cm-2)	60	297	256	543
Capacitance (F.cm-2)		1.50E-09	1.60E-06	0.13

The evolution of the electrochemical performance of the electrolyte with temperature has been measured under wet air and dry hydrogen. From each temperature it is possible to calculate the bulk, grain boundary and total conductivity of the electrolyte, using equation [5].

$$\sigma_e = \frac{e_{electrolyte}}{R_{mes}*Surface} \qquad [5]$$

Where σ_e is the electrolyte conductivity in S.cm^{-1} at at the operating temperature, e the thickness of the electrolyte in cm and S the surface of the electrolyte in cm. After the extraction of all the conductivities at several operating temperatures it is possible to draw an Arrhenius diagram of the conductivity dependence to the temperature. Using the slope of this Arrhenius relation, it is possible to determine the activation energy of the reaction following equation [6].

$$E_a = \frac{a*1000* \, k_b*\ln(10)}{e} \qquad [6]$$

Where E_a is the activation energy in eV, a the slope of the liner fit, K_b the Boltzmann constant in m^2 kg s^{-2} K^{-1}.

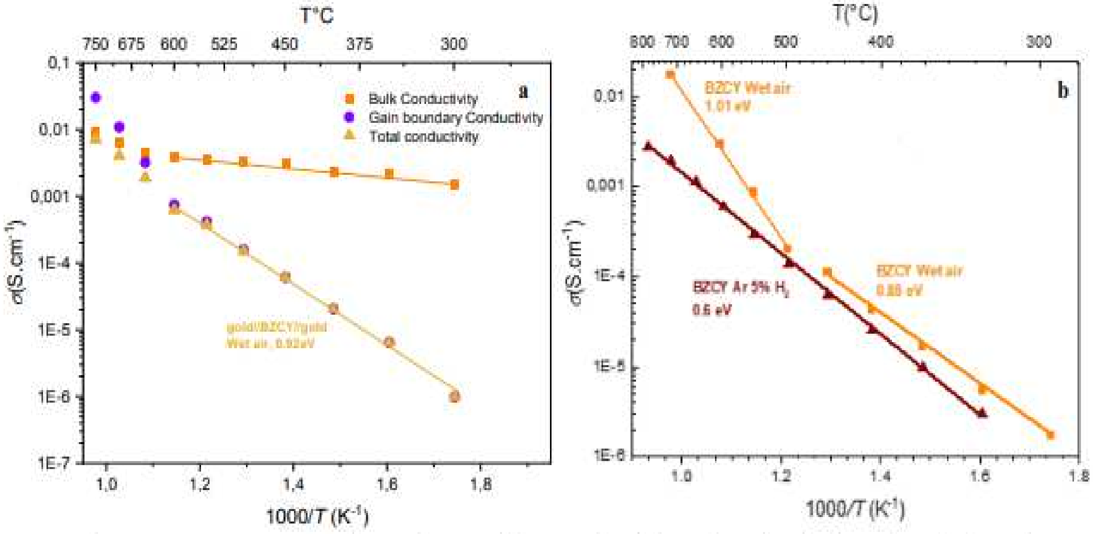

Figure 10. Temperature dependence of the conductivity related to bulk and grain boundary (a) and to total conductivity under different atmospheres (b)

The Arrhenius diagram of Figure 10a shows that at temperatures lower than 600°C, the total conductivity is driven by the grain boundary contribution. However, at higher temperature, there is a variation in the activation energy which might indicate the presence of a more complex conductivity. Figure 10b shows total conductivity of the electrolyte under different atmospheres and can be compared to the literature (28) when the electrolyte is associated to different electrodes. Under 5% H_2, the activation energy is the same in the whole temperature range, whereas it is not the same under air and the sample under wet air it is possible to observe the activation energy variation in accordance with literature (28). Moreover, $BaZr_{0.7}Ce_{0.2}Y_{0.1}O_{3-\delta}$ samples synthetized expels conductivities an order of magnitude lower than the ones present in the literature.

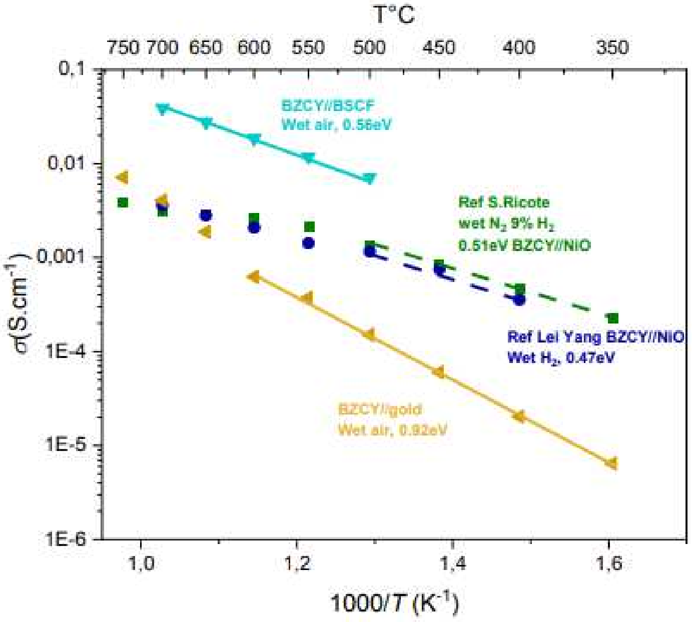

Figure 11. Temperature dependence of the conductivity, of the $BaZr_{0.7}Ce_{0.2}Y_{0.1}O_{3-\delta}$(BZCY) electrolyte, comparison between gold and BSCF air-electrode

All the measurements have been done using gold electrodes, however, gold does not get along ceramics very well. Delamination of these electrodes can be observed after the measurements. This is the reason why the materials used has been replaced by $Ba_{0.5}Sr_{0.5}Co_{0.8}Fe_{0.2}O_{3-\delta}$. The $Ba_{0.5}Sr_{0.5}Co_{0.8}Fe_{0.2}O_{3-\delta}$ is known to be one of the best air-electrode for Barium based ceramic electrolytes (29). Figure 11 shows the Arrhenius diagram that compares the conductivity of the $BaZr_{0.7}Ce_{0.2}Y_{0.1}O_{3-\delta}$ symmetrical cell with gold electrodes and $Ba_{0.5}Sr_{0.5}Co_{0.8}Fe_{0.2}O_{3-\delta}$ electrodes. It is possible to observe that at 600°C the electrolyte expels a conductivity two orders of magnitude higher than with the gold. Therefore, for further measurements, gold should be avoided as an electrode for symmetrical cells. Moreover, results obtained using the $Ba_{0.5}Sr_{0.5}Co_{0.8}Fe_{0.2}O_{3-\delta}$ with the $BaZr_{0.7}Ce_{0.2}Y_{0.1}O_{3-\delta}$ electrolyte are very promising and will be developed in future works.

CONCLUSION AND PERSPECTIVES

In this study the zirconium-rich $BaZr_{0.7}Ce_{0.2}Y_{0.1}O_{3-\delta}$ electrolyte material has been synthetized using the auto-combustion process. The powder obtained has been purified and shaped into an electrolyte. The electrolyte material has been characterized using various technics. The densification behavior of the zirconium rich phase has been explored and compared to the cerium rich phase. The complete densification of the $BaZr_{0.7}Ce_{0.2}Y_{0.1}O_{3-\delta}$ occurred at very high temperature (1600°C). The reduction of this very high sintering temperature using cold sintering process has been attempted. Unfortunately, it has been shown that the CSP protocol used on cerium rich $BaZr_{0.3}Ce_{0.6}Y_{0.1}O_{3-\delta}$ had limited application and must be adapted to the zirconium rich $BaZr_{0.7}Ce_{0.2}Y_{0.1}O_{3-\delta}$. A complete crystallographic study of the solid solution of the $BaZr_{x}Ce_{1-x}Y_{0.1}O_{3-\delta}$ material has been achieved, and for the first time, it has been showed that the densification limitation could be linked to the segregation of the crystallographic structure of the material. Different synthesis process and characterization technics will be used in further work to identify the possible presence of a miscibility gap inside the $BaZr_{x}Ce_{1-x}Y_{0.1}O_{3-\delta}$ solid solution.

After sintering at 1600°C, the conductivity of the $BaZr_{0.7}Ce_{0.2}Y_{0.1}O_{3-\delta}$ has been characterized by EIS measurements. The electrolyte material has been tested in symmetrical cells, and promising results of 10^{-2} $S.cm^{-1}$ at 500°C were obtained using $Ba_{0.5}Sr_{0.5}Co_{0.8}Fe_{0.2}O_{3-\delta}$ electrodes. For future work, the study of other densification process, using sintering aids or flash sintering could help to lower the densification temperature and the conductivity of the $BaZr_{0.7}Ce_{0.2}Y_{0.1}O_{3-\delta}$ material.

Acknowledgments

This work is part of ARCADE Franco German ANR/BMBF project (ANR-19-ENR-0003) "Advanced and Robust metal supported Cell with proton conducting ceramic for electrolysis Applications in defossilized Energy systems"

References

(1) Hiroyasu Iwahara. ‘Proton Conducting Ceramics and Their Applications’. *Solid State Ionics* 86–88 (July 1996): 9–15. https://doi.org/10.1016/0167-2738(96)00087-2.

(2) Sefiu Abolaji Rasaki, Changyong Liu, Changshi Lao, and Zhangwei Chen. ‘A Review of Current Performance of Rare Earth Metal-Doped Barium Zirconate Perovskite: The Promising Electrode and Electrolyte Material for the Protonic Ceramic Fuel Cells’. *Progress*

in Solid State Chemistry 63 (September 2021): 100325. https://doi.org/10.1016/j.progsolidstchem.2021.100325.

(3) Francisco J.A. Loureiro, Narendar Nasani, G. Srinivas Reddy, N.R. Munirathnam, and Duncan P. Fagg. ‘A Review on Sintering Technology of Proton Conducting BaCeO3-BaZrO3 Perovskite Oxide Materials for Protonic Ceramic Fuel Cells’. *Journal of Power Sources* 438 (October 2019): 226991. https://doi.org/10.1016/j.jpowsour.2019.226991.

(4) A.Boudghene Stambouli and E Traversa. ‘Solid Oxide Fuel Cells (SOFCs): A Review of an Environmentally Clean and Efficient Source of Energy’. *Renewable and Sustainable Energy Reviews* 6, no. 5 (October 2002): 433–55. https://doi.org/10.1016/S1364-0321(02)00014-X.

(5) Michael C. Tucker, ‘Progress in Metal-Supported Solid Oxide Fuel Cells: A Review’. *Journal of Power Sources* 195, no. 15 (August 2010): 4570–82. https://doi.org/10.1016/j.jpowsour.2010.02.035.

(6) H. Iwahara, ‘Technological Challenges in the Application of Proton Conducting Ceramics’. *Solid State Ionics* 77 (April 1995): 289–98. https://doi.org/10.1016/0167-2738(95)00051-7.

(7) K. Kreuer, ‘On the Complexity of Proton Conduction Phenomena’. *Solid State Ionics* 136–137, no. 1–2 (2 November 2000): 149–60. https://doi.org/10.1016/S0167-2738(00)00301-5.

(8) Y. Huang, R. Merkle, and J. Maier. ‘Effect of NiO Addition on Proton Uptake of BaZr1-XYxO3-x/2 and BaZr1-XScxO3-x/2 Electrolytes’. *Solid State Ionics* 347 (April 2020): 115256. https://doi.org/10.1016/j.ssi.2020.115256.

(9) Hye-Won Kim, Jun Seo, Ji Haeng Yu, Kyong Sik Yun, Jong Hoon Joo, Jooho Moon, and Hee Jung Park. ‘Effect of Cerium on Yttrium-Doped Barium Zirconate with a ZnO Sintering Aid: Grain and Grain Boundary Protonic Conduction’. *Ceramics International* 47, no. 23 (December 2021): 32720–26. https://doi.org/10.1016/j.ceramint.2021.08.168.

(10) Nur Lina Rashidah Mohd Rashid, Abdullah Abdul Samat, Abdul Azim Jais, Mahendra Rao Somalu, Andanastuti Muchtar, Nurul Akidah Baharuddin, and Wan Nor Roslam Wan Isahak. ‘Review on Zirconate-Cerate-Based Electrolytes for Proton-Conducting Solid Oxide Fuel Cell’. *Ceramics International* 45, no. 6 (April 2019): 6605–15. https://doi.org/10.1016/j.ceramint.2019.01.045.

(11) K. Kreuer, ‘Aspects of the Formation and Mobility of Protonic Charge Carriers and the Stability of Perovskite-Type Oxides’. *Solid State Ionics* 125, no. 1–4 (October 1999): 285–302. https://doi.org/10.1016/S0167-2738(99)00188-5.

(12) Rotraut Merkle, Maximilian F. Hoedl, Giulia Raimondi, Reihaneh Zohourian, and Joachim Maier. ‘Oxides with Mixed Protonic and Electronic Conductivity’. *Annual Review of Materials Research* 51, no. 1 (26 July 2021): 461–93. https://doi.org/10.1146/annurev-matsci-091819-010219.

(13) Pattaraporn Kim-Lohsoontorn and Joongmyeon Bae. ‘Electrochemical Performance of Solid Oxide Electrolysis Cell Electrodes under High-Temperature Coelectrolysis of Steam and Carbon Dioxide’. *Journal of Power Sources* 196, no. 17 (September 2011): 7161–68. https://doi.org/10.1016/j.jpowsour.2010.09.018.

(14) K. Otsuka, M. Hatano and, A. Morikawa ‘Hydrogen from Water by Cerium Reduction’ Journal of Catalysis 79, 493-496 (1983)

(15) R. R. Chien, V. Hugo Schmidt, S.-C. Lee, C.-C. Huang, and Stachus P. Tu. ‘Glycine-Nitrate Synthesis and Characterization of Ba(Zr0.8-XCexY0.2)O2.9’. In *Ceramic Engineering and Science Proceedings*, edited by Narottam P. Bansal, Prabhakar Singh, Dileep Singh, and Jonathan Salem, 239–48. Hoboken, NJ, USA: John Wiley & Sons, Inc., 2010. https://doi.org/10.1002/9780470584316.ch23.

(16) Alexander S. Mukasyan, Colleen Costello, Katherine P. Sherlock, David Lafarga, and Arvind Varma. ‘Perovskite Membranes by Aqueous Combustion Synthesis: Synthesis and

Properties'. *Separation and Purification Technology* 25, no. 1–3 (October 2001): 117–26. https://doi.org/10.1016/S1383-5866(01)00096-X.

(17) Stefan Jianhua Tong Nikodemski and Ryan O'Hayre. 'Solid-State Reactive Sintering Mechanism for Proton Conducting Ceramics'. *Solid State Ionics* 253 (December 2013): 201–10. https://doi.org/10.1016/j.ssi.2013.09.025.

(18) Gordon B. Skinner, and Herrick L. Johnston. 'Thermal Expansion of Zirconium between 298°K and 1600°K'. *The Journal of Chemical Physics* 21, no. 8 (August 1953): 1383–84. https://doi.org/10.1063/1.1699227.

(19) X. Kuang, G. Carotenuto, and L. Nicolais. 'A Review of Ceramic Sintering and Suggestions on Reducing Sintering Temperatures', 1997, 18.

(20) Ji Li, Chao Wang, Xianfen Wang, and Lei Bi. 'Sintering Aids for Proton-Conducting Oxides – A Double-Edged Sword? A Mini Review'. *Electrochemistry Communications* 112 (March 2020): 106672. https://doi.org/10.1016/j.elecom.2020.106672.

(21) Salvatore Grasso, Mattia Biesuz, Luca Zoli, Gianmarco Taveri, Andrew I. Duff, Daoyao Ke, Anna Jiang, and Michael J. Reece. 'A Review of Cold Sintering Processes'. *Advances in Applied Ceramics* 119, no. 3 (2 April 2020): 115–43. https://doi.org/10.1080/17436753.2019.1706825.

(22) Hanzheng Guo, Jing Guo, Amanda Baker, and Clive A. Randall. 'Hydrothermal-Assisted Cold Sintering Process: A New Guidance for Low-Temperature Ceramic Sintering'. *ACS Applied Materials & Interfaces* 8, no. 32 (17 August 2016): 20909–15. https://doi.org/10.1021/acsami.6b07481.

(23) K. Thabet, E. Quarez, O. Joubert, and A. Le Gal La Salle. 'Application of the Cold Sintering Process to the Electrolyte Material BaCe0.8Zr0.1Y0.1O3-δ'. *Journal of the European Ceramic Society* 40, no. 9 (August 2020): 3445–52. https://doi.org/10.1016/j.jeurceramsoc.2020.03.043.

(24) S. Raz, K. Sasaki, J. Maier, and I. Riess. 'Characterization of Adsorbed Water Layers on Y2O3-Doped ZrO2', 2001, 24.

(25) Kawther Thabet. Phd Manuscript, 'Pile à combustible à céramique conductrice protonique : élaboration et caractérisations physico-chimiques et électrochimiques des matériaux et optimisation de la mise en forme par le procédé de densification à basse température CSP', Université de Nantes-Institut de matériaux de Nantes Jean-Rouxel, n.d., 218.

(26) D. Jennings, S. Ricote, J. Santiso, and I. Reimanis. 'The Formation of Oriented Barium Carbonate from the Decomposition of Yttria-Doped Barium Zirconate Films'. *Scripta Materialia* 186 (September 2020): 401–5. https://doi.org/10.1016/j.scriptamat.2020.05.028.

(27) Bernard Lesage, 'Some Aspects of Diffusion in Ceramics'. *Journal de Physique III* 4, no. 10 (October 1994): 1833–50. https://doi.org/10.1051/jp3:1994243.

(28) S. Ricoteand, N. Bonanos. 'Enhanced Sintering and Conductivity Study of Cobalt or Nickel Doped Solid Solution of Barium Cerate and Zirconate'. *Solid State Ionics* 181, no. 15–16 (3 June 2010): 694–700. https://doi.org/10.1016/j.ssi.2010.04.007.

(29) Wei Zhou, Ran Ran, and Zongping Shao. 'Progress in Understanding and Development of Ba0.5Sr0.5Co0.8Fe0.2O3−δ-Based Cathodes for Intermediate-Temperature Solid-Oxide Fuel Cells: A Review'. *Journal of Power Sources* 192, no. 2 (15 July 2009): 231–46. https://doi.org/10.1016/j.jpowsour.2009.02.069.